Journal of Insights in Basic and Applied Sciences
مجلة رؤى في العلوم الأساسية والتطبيقية
ISSN: 3106-1737
Volume 2, Issue 4, 2026, Pages: 586-595
Journal homepage: https://jibas.com.ly/index.php/jibas/en

Comparative Analysis of the Thermal, Electrical, and Structural Properties of Sulfate-Doped Glycine Crystals Grown by Slow Evaporation: Predictive Selection Rules for Application-Specific Doping

Ollaa M. Mailoud[1,3], Zeinab Algadhi[2,3], Nadir Omar Massoud Driza[1]*
[1]Department of Physics, Faculty of Science Almarj, University of Benghazi, Libya
[2]General Department, Faculty of Science, University of Benghazi, Libya
[3]Physics Research Group (PRG)

تحليل مقارن للخصائص الحرارية والكهربائية والهيكلية لبلورات الجليسين المطعمة بالكبريتات والمُنمّاة بطريقة التبخير البطيء: قواعد اختيار تنبؤية للتطعيم الموجه لتطبيقات محددة

علا مفتاح ميلود[1،3]، زينب صالح القاضي[2،3]، نادر عمر مسعود ادريزه[1*]
[1]قسم الفيزياء، كلية العلوم المرج، جامعة بنغازي، المرج، ليبيا
[2]قسم الفيزياء، كلية العلوم ، جامعة بنغازي، بنغازي، ليبيا
[3]مجموعة أبحاث الفيزياء، بنغازي، ليبيا

* Corresponding author: nadir.driza@uob.edu.edu

Received: *September 20, 2026*	Accepted: *October 26, 2026*	Published: November 26

Copyright: © 2026 by the authors. This article is an open-access article distributed under the terms and conditions of the Creative Commons Attribution (CC BY) license (https://creativecommons.org/licenses/by/4.0/).

Abstract
Glycine crystallizes in three polymorphs, of which only the γ phase ($P3_1$) is non-centrosymmetric and therefore second-order nonlinear-optically active. Yet the growth of device-grade crystals is hampered by polymorphic competition, modest thermal margins, and uncontrolled dielectric loss. This paper develops a unified theoretical framework that compares the structural, thermal, and electrical responses of glycine crystals doped with dilute sulfate salts (Mg^{2+}, Zn^{2+}, Ni^{2+}, Cu^{2+}, and alkali/ammonium sulfates) grown by slow evaporation. Dopant incorporation is treated through three crystallochemical channels proton-transfer adduct formation, carboxylate-coordinated metal–sulfate defect pairs, and interlayer insertion of oversized cations and their consequences are propagated through twelve quantitative relations covering lattice distortion, decomposition kinetics, and frequency-dependent conductivity. The analysis resolves the scattered literature into explicit selection rules: divalent first-row sulfate dopants in the sub-2 mol% regime preserve the polar γ lattice while raising the decomposition onset and suppressing dielectric loss, whereas the stoichiometric glycine–sulfuric acid branch yields triglycine-sulfate-type ferroelectrics optimized for pyroelectric detection below 49 °C. Because a single dopant cannot simultaneously optimize all three property families, Mg^{2+}/Zn^{2+} sulfate-doped γ-glycine is promoted for nonlinear optical frequency conversion, Ni^{2+}/Mg^{2+}-doped crystals for low-loss dielectric microstructures, and TGS-type adducts for pyroelectric infrared detection each to the exclusion of the other dopant classes.

Keywords: glycine single crystals; sulfate doping; slow evaporation technique; γ-glycine; dielectric relaxation; thermal decomposition; nonlinear optical materials; semiorganic crystals

الملخص
يتبلور الجليسين في ثلاثة أشكال متعددة، منها الطور ($P3_1$) γ فقط غير متناظر مركزيًا، وبالتالي فهو نشط بصريًا غير خطي من الدرجة الثانية. ومع ذلك، فإن نمو البلورات ذات الجودة المناسبة للأجهزة يعيقه التنافس بين الأشكال المتعددة، والهوامش الحرارية المحدودة، وفقدان العزل الكهربائي غير المنضبط. تقدم هذه الورقة إطارًا نظريًا موحدًا يقارن الاستجابات البنيوية والحرارية والكهربائية لبلورات الجليسين المطعمة بأملاح الكبريتات المخففة(Mg^{2+} ، Zn^{2+}، Ni^{2+}، Cu^{2+}، وكبريتات القلويات/الأمونيوم) التي تم إنماؤها عن طريق التبخير البطيء. تُعالج عملية إدخال الشوائب من خلال ثلاث قنوات بلورية كيميائية: تكوين نواتج إضافة نقل البروتون، وأزواج عيوب الكبريتات المعدنية المنسقة مع الكربوكسيلات، وإدخال الكاتيونات كبيرة الحجم بين الطبقات، وتُعمم نتائجها من خلال اثنتي عشرة علاقة كمية تغطي تشوه الشبكة البلورية، وحركية التحلل، والتوصيلية المعتمدة على التردد. يُلخص التحليل ما ورد في الأدبيات المتناثرة في قواعد اختيار واضحة: تحافظ شوائب الكبريتات ثنائية التكافؤ من الصف الأول، بتركيز أقل من 2% مول، على الشبكة البلورية القطبية γ مع رفع بداية التحلل وكبح الفقد العازل، بينما ينتج عن فرع الجليسين-حمض الكبريتيك المتكافئ مواد كهرضغطية من نوع كبريتات ثلاثي الجليسين مُحسَّنة للكشف الكهروحراري عند درجات حرارة أقل من 49 درجة مئوية. نظرًا لأن مادة التطعيم الواحدة لا يمكنها تحسين جميع عائلات الخصائص الثلاث في وقت واحد، يتم الترويج لـ-γ جليسين المطعّم بكبريتات Mg^{2+}/Zn^{2+} لتحويل التردد البصري غير الخطي، والبلورات المطعّمة بـ Ni^{2+}/Mg^{2+} للهياكل الدقيقة العازلة منخفضة الفقد، والمواد المضافة من نوع TGS للكشف الكهروحراري بالأشعة تحت الحمراء، كل منها على حساب فئات مواد التطعيم الأخرى.

الكلمات المفتاحية: بلورات أحادية من الجليسين؛ تطعيم بالكبريتات؛ تقنية التبخر البطيء؛ جليسين غاما؛ الاسترخاء العازل؛ التحلل الحراري؛ مواد بصرية غير خطية؛ بلورات شبه عضوية.

1. Introduction

The search for efficient, mechanically robust, and thermally stable photonic and dielectric materials has established the semiorganic family of crystals, in which the high nonlinear optical (NLO) and structural flexibility of organic molecules are combined with the ionic cohesion of inorganic moieties [1] [2]. The compounds such as zinc tris (thiourea) sulfate (ZTS) [3] and bis(thiourea) cadmium chloride [4] [5] have confirmed that Synthesized organic–inorganic hybrids can outperform either parent class in frequency-conversion devices. It is clearly seen that glycine (NH_2CH_2COOH) holds a unique position; it is inexpensive - despite its crystals representing the simplest of all amino acids - and exists as a zwitterion. Furthermore, it forms crystal lattices interconnected by hydrogen bonds, the polarity of which can be altered by selecting different polymorphic forms [6] or by incorporating specific ions.

Glycine crystallizes in three well-characterized polymorphs: the non-centrosymmetric γ phase ($P3_1$) [6] [7], the centrosymmetric α phase ($P2_1/n$) [8], and the metastable β phase ($P2_1$) [9]; the structures have been refined to high precision [10] and are indexed in the standard powder-diffraction files[11]. Only the γ phase lacks an inversion centre and therefore exhibits an electric-dipole second-order nonlinear optical (NLO) response, whereas the α phase is second-harmonic-generation (SHG) [1] inactive by symmetry. Because the β phase crystallizes only under kinetic control, the practical growth problem reduces to obtaining large, strain-free γ crystals historically difficult because nucleation competition favours α in pure aqueous solution [12].

Sulfate occupies a unique position among glycine dopants. The stoichiometric glycine–sulfuric acid compound triglycine sulfate (TGS) [13], discovered more than six decades ago[14] [15] and structurally resolved shortly afterwards [16], remains a reference ferroelectric and pyroelectric detector material [15,17,18]. Sulfate therefore interacts with glycine [19] through chemically well-understood channels rather than by accidental inclusion. Nevertheless, the literature on sulfate-doped glycine crystals grown by slow evaporation remains fragmented [19]: individual salts ($MgSO_4$, $ZnSO_4$, $NiSO_4$, $CuSO_4$, K_2SO_4, $(NH_4)_2SO_4$) are reported in isolated case studies, structural, thermal, and electrical properties are measured separately, and no unified framework connects dopant chemistry to the coupled property triad.

This paper provides a critical theoretical synthesis and perspective roadmap. By mapping the three crystallochemical incorporation channels of sulfate onto quantitative models for lattice microstrain, kinetic decomposition, and frequency-dependent dielectric dispersion, we establish predictive selection rules for functional applications. The perspective presented here is explicitly prescriptive: to provide experimentalists with theoretical selection criteria that identify optimal dopant regimes and highlight non-viable compositions prior to empirical synthesis.

2. Research Problem, Objective, and Significance

The research problem can be stated as an optimization question: for a given target application, which dilute sulfate dopant maximizes the coupled structural–thermal–electrical figure of merit of slow-evaporation-grown glycine crystals? Three subordinate questions must be answered. First, through which crystallochemical channel does each sulfate salt enter the glycine lattice, and what lattice distortion does it generate? Second, how do the resulting defects propagate into decomposition kinetics and dielectric relaxation? Third, which dopant–concentration regime matches which device application?

The significance is twofold. Scientifically, the analysis converts scattered case reports into a falsifiable property-regime map with twelve quantitative relations testable by a single experimental campaign: powder or single-crystal X-ray diffraction, infrared spectroscopy, thermogravimetric analysis at several heating rates, and dielectric spectroscopy from 10 Hz to 1 MHz. Technologically, the framework motivates the adoption of specific doped crystals and the exclusion of

others for nonlinear optical frequency conversion, pyroelectric infrared detection, and low-loss dielectric microstructures, for which undoped or wrongly doped glycine underperforms.

3. Crystal Chemistry of Glycine and Sulfate Incorporation

3.1 Polymorphism and polarity

Table 1 summarizes the polymorphic basis of the analysis. The α phase packs zwitterions in antiparallel double layers, cancelling molecular dipoles; the γ phase arranges head-to-tail glycine chains into 3_1 helices along the c-axis, so that hydrogen-bond dipoles add constructively and a macroscopic polar axis results [7,8,20]. This topological difference is the symmetry foundation of every application discussed below: polarity gives piezoelectricity, pyroelectricity, and SHG, while the denser three-dimensional hydrogen-bond network of γ is also the origin of its superior thermal robustness [7,20].

Table 1. Crystallographic comparison of the glycine polymorphs (structural data from refs. [7–10]; indexing per ICDD cards [11]).

Phase	Space group	Lattice parameters	Z	Density (g cm^{-3})	Symmetry and consequence
A	$P2_1/n$	a = 5.105 Å, b = 11.968 Å, c = 5.466 Å, β = 111.6° [5]	4	1.607	Centrosymmetric — electric-dipole SHG forbidden
β	$P2_1$	a = 5.09 Å, b = 6.17 Å, c = 5.32 Å, β = 112.3° [6]	2	≈1.59	Polar but metastable; kinetic product, avoided for devices
Γ	$P3_1$	a = b = 7.035 Å, c = 5.481 Å [4]	3	1.596	Non-centrosymmetric polar (c-axis) — SHG active; most robust H-bond network

3.2 Incorporation channels of sulfate

Sulfate incorporation proceeds through three channels with distinct structural consequences. Channel (i) is proton-transfer adduct formation, Eq. (1): at stoichiometric acid content the solution crystallizes its own compound, a TGS-type adduct containing two zwitterions, one glycinium cation, and one hydrogen-sulfate anion per formula unit, exactly as resolved for TGS [13,15,16]. This channel produces a new crystal rather than a doped glycine crystal, and is treated in Section 7 as a separate materials branch.

$$3\,\mathrm{Gly0} + H_2SO_4 \rightarrow (\mathrm{GlyH^+})(\mathrm{Gly^\pm})_2 \cdot HSO_4^- \quad (1)$$

where $Gly^0 = NH_2CH_2COOH$ (neutral glycine), $Gly^\pm = NH_3^+CH_2COO^-$ (zwitterion), and $GlyH^+ = NH_3^+CH_2COOH$ (glycinium); the ionic distribution follows the TGS structure [13,14,15,16].

Channel (ii) is the metal–sulfate defect pair: divalent cations (Mg^{2+}, Zn^{2+}, Ni^{2+}, Cu^{2+}) coordinate carboxylate oxygen atoms, while the sulfate tetrahedron acts as a strong hydrogen-bond acceptor for neighbouring NH_3^+ groups; the pair is charge-neutral and therefore requires no additional lattice compensation. Nevertheless, owing to differences in effective ionic radii and local coordination geometry around the divalent cation, each $[M^{2+} \ldots SO_4^{2-}]$ pair generates a localized lattice distortion field that perturbs neighboring hydrogen bonds, thereby accounting for the onset of measurable microstrain (ε_{str}) when dopant concentrations exceed ≈ 1 mol% (Section 4). Channel (iii) applies to oversized alkali or ammonium cations: because their six-coordinate ionic radii (1.38–1.43 Å [19,21]) exceed any glycine lattice void, they insert between hydrogen-bonded layers and compete for N–H···O bonds, expanding the interlayer spacing. Throughout this work "dilute" is defined as a dopant feed below 2 mol% in the mother liquor, the regime in which the doped crystal retains a single diffraction phase (Section 4) and all dopant effects can be treated as point-defect physics rather than phase formation.

3.3 Growth by slow evaporation

Growth by slow evaporation of aqueous solutions is the enabling technique because it maintains near-equilibrium conditions. The supersaturation, Eq. (2), remains low (typically S = 1.01–1.05) when solvent is removed over weeks at ambient temperature, minimizing solution-mediated defect capture and yielding well-faceted crystals [22]. Slight acidification (pH 2–4) partially protonates dissolved glycine and, in the presence of sulfate-bearing solutes, biases nucleation towards the γ phase, as exploited in the growth of pure γ-glycine [12,20]. Growth-rate anisotropy follows the qualitative law $R \propto (S - 1)g$, where g is the growth exponent, so morphological stability is preserved at the low supersaturations of this technique [22] as it seen in this equation

$$S = C/C^* \geq 1 \quad (2)$$

where C is the actual solute concentration and C* the equilibrium solubility at the growth temperature [22].

4. Comparative Structural Properties

The structural comparison rests on four standard relations applied to powder X-ray diffraction (XRD). The mean crystallite size D follows the Scherrer equation, Eq. (3) [23,24,25] as the following:

$$D = K\lambda / (\beta \cos \theta) \tag{3}$$

where $K \approx 0.9$, λ is the Cu Kα wavelength (1.5406 Å), and β is the instrumental-corrected integral peak breadth.

The Size and strain contributions are separated by the Williamson–Hall relation, Eq. (4) [25,26] as the following:

$$\beta \cos \theta = K\lambda/D + 4\, \varepsilon_{str} \sin \theta \tag{4}$$

from which the microstrain ε_{str} is obtained from the slope of $\beta\cos\theta$ versus $\sin\theta$. The dislocation density, Eq. (5) [27], quantifies the defect content of the growth front, and dopant-induced interplanar-spacing changes follow the differential Bragg relation, Eq. (6) [27] as the following:

$$\delta = 1/D^2 \tag{5}$$

$$\Delta d/d \approx -\Delta\theta \cdot \cot \theta \tag{6}$$

Applying these relations to the dopant channels of Section 3 yields testable predictions, classified in Table 2 by the effective ionic radii of Shannon [21] and visualized in Fig. 1. Divalent first-row cations (Ni^{2+} 0.69 Å, Mg^{2+} 0.72 Å, Cu^{2+} 0.73 Å, Zn^{2+} 0.74 Å) fit within the hydrogen-bonded network when coordinated by carboxylate oxygen; at feed levels of 0.5–1 mol% they are predicted to sharpen reflections (β decreases, D increases, δ decreases) because compatible impurities suppress spurious nucleation and let the growth front anneal, whereas beyond ≈1 mol% strain accumulation broadens the reflections again. Cu^{2+} is the exception: its Jahn–Teller-active d^9 configuration produces anisotropic, tetragonally elongated coordination, so broadening appears earlier and preferentially on specific hkl families. Alkali and ammonium sulfates produce the opposite signature measurable $\Delta d/d$ shifts and preferred orientation because interlayer insertion directly strains the spacing of the hydrogen-bonded sheets. In every dilute divalent case the pattern must remain single-phase and indexable against the glycine cards [11]; the appearance of additional reflections marks exit from the dilute regime defined in Section 3.

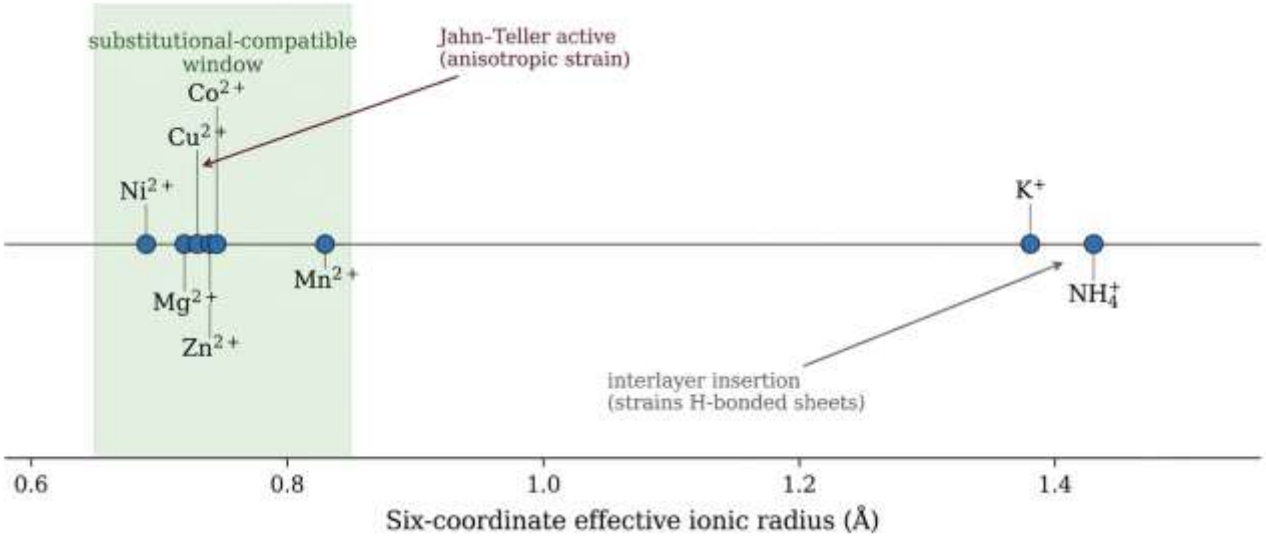


Figure 1: Classification of candidate sulfate dopants by six-coordinate effective ionic radius (data from Shannon [21]). Cations within the shaded 0.65–0.85 Å window (Ni^{2+}, Mg^{2+}, Cu^{2+}, Zn^{2+}, Co^{2+}, Mn^{2+}) act as carboxylate-coordinated point defects in the glycine network, whereas oversized K^+ and NH_4^+ insert between the hydrogen-bonded layers. The Jahn–Teller-active Cu^{2+} ion adds anisotropic strain within the window.

Infrared spectroscopy provides the chemical fingerprint of the incorporation channel. Sulfate exhibits its characteristic internal modes near 980 cm^{-1} (ν_1), 450 cm^{-1} (ν_2), 1100–1140 cm^{-1} (ν_3), and 610–620 cm^{-1} (ν_4) [28,29]; detection of these bands in doped crystals confirms sulfate presence, while their splitting and shift report on site symmetry. Strengthening of the N–H···O–S interaction shifts the NH_3^+ deformation and COO^- stretching bands (near 1510, 1410, and 1610 cm^{-1}) in the direction expected for stronger hydrogen bonding [28]. The combination of single-phase XRD and sulfate-band FTIR therefore constitutes the structural acceptance test for the dilute regime.

Table 2. Predicted structural response of slow-evaporation-grown glycine crystals to the sulfate dopant classes (theoretical expectations of Sections 3–4; radii from Shannon [21]).

Dopant class	r(M^{n+}) (Å) [14]	Incorporation site	Expected XRD signature	Expected FTIR signature
Divalent first-row sulfates (Ni^{2+}, Mg^{2+}, Zn^{2+})	0.69–0.74	Carboxylate-coordinated $\{M^{2+}\cdots SO_4^{2-}\}$ defect pair	Single phase; minimal Δd/d; FWHM and δ minima near 0.5–1 mol%; broadening above ≈1 mol% (Eqs. (4)–(6))	$\nu_3(SO_4^{2-})$ 1100–1140 cm^{-1}, ν_4 610–620 cm^{-1} [28]; NH_3^+/COO^- shifts indicating stronger N–H···O–S bonds
$CuSO_4$ (Jahn–Teller d^9)	0.73	Same, with tetragonally elongated coordination	Anisotropic, hkl-dependent broadening at lower feed levels	Sulfate modes as above; possible Cu–O carboxylate contribution overlapping ν_4
Alkali/ammonium sulfates (K_2SO_4, $(NH_4)_2SO_4$)	1.38–1.43	Interlayer insertion; competes for N–H···O bonds	Measurable Δd/d (Eq. (6)); preferred orientation; strain broadening	Sulfate modes present; weakened, shifted NH_3^+ deformation band
Stoichiometric H_2SO_4 (proton-transfer branch)	—	Own compound: TGS-type adduct, Eq. (1)	New phase; pattern indexes to a TGS-type cell, not to glycine cards [8]	Strong ν_1–ν_4 sulfate envelope; glycinium NH_3^+ bands

5. Comparative Thermal Properties

Thermogravimetric analysis (TGA) and differential scanning calorimetry (DSC) compare the doped crystals on three observables: the dehydration signature, the decomposition onset, and the decomposition activation energy. Pure glycine decomposes at approximately 233 °C, with reported onsets spanning 233–262 °C depending on polymorph and heating rate [6,7,8]; the γ phase consistently exhibits the highest robustness owing to its three-dimensional hydrogen-bond network [7].

Dopant physics predicts three distinct thermal responses. First, coordinated divalent sulfates introduce ionic cross-links one M–O coordination bond plus two strong N–H···O–S hydrogen bonds per defect which raise the effective bond-breaking energy and shift the decomposition onset upward; the effect should scale with cation field strength and be strongest for Mg^{2+} and Zn^{2+}. Second, hydrated feed salts (for example $MgSO_4{\cdot}7H_2O$ and $ZnSO_4{\cdot}7H_2O$) contribute endothermic dehydration events in the 60–120 °C window that must be distinguished from lattice-water loss; growth from pre-dried, filtered solutions suppresses occluded hydrates. Importantly, any residual occluded solvent molecules trapped within the crystal lattice during slow evaporation do not merely produce low-temperature thermal mass-loss signatures, but can also act as dipolar and proton-conducting impurities that artificially elevate the low-frequency dielectric dissipation factor ($\tan\delta$) in subsequent electrical measurements (Section 6). Third, the stoichiometric glycine–sulfuric acid branch crystallizes TGS-type adducts whose ferroelectric Curie point at 49 °C [15,17,18] does not threaten chemical stability but caps the ferroelectric operating window, a distinction elaborated in Sections 6 and 7.

Decomposition kinetics are quantified by the Kissinger method, Eq. (7) [30,31]: from the heating-rate dependence of the peak temperature T_p, the decomposition activation energy E_d is extracted. The framework predicts the ordering E_d(dilute $Mg^{2+}/Zn^{2+}/Ni^{2+}$ sulfate) > E_d(pure γ) ≈ E_d(Cu^{2+}-doped) > E_d(alkali-inserted), because the first group strengthens and the last group weakens the bond network that must fail during decomposition. Thermal analysis at no fewer than three heating rates is therefore prescribed as the experimental discriminator, and any dopant whose E_d does not exceed that of pure γ-glycine should be rejected for thermally demanding applications.

$$\ln\left(\frac{\beta_h}{T_p^2}\right) = -\frac{E_d}{RT_p} + \text{const} \qquad (7)$$

where β_h is the heating rate, R the gas constant, and T_p the absolute temperature of the DSC/TGA peak [30].

6. Comparative Electrical Properties

The electrical comparison uses the parallel-plate relations for the relative permittivity, Eq. (8), and for the alternating-current (AC) conductivity, Eq. (9), where C is the measured capacitance, t the specimen thickness, A the electrode area, f the frequency, and tanδ the dissipation factor. Four polarization mechanisms contribute in decreasing order of response speed: electronic, ionic, dipolar (Debye-type) [32], and interfacial Maxwell–Wagner–Sillars (MWS) polarization arising at heterogeneous, dopant-rich regions [33–35]. The dopant question is therefore not only how much polarization each channel adds, but at which frequency and temperature it relaxes.

$$\varepsilon_r = C\, t / (\varepsilon_0 A) \quad (8)$$

$$\sigma_{ac} = 2\pi f\, \varepsilon_0\, \varepsilon_r \tan\delta \quad (9)$$

In the dilute divalent regime, the $\{M^{2+}\cdots SO_4^{2-}\}$ defect pair is charge-neutral and immobile; it pins formerly ionizable groups and reduces the free-carrier population that dominates low-frequency loss. The predicted dielectric signature is a modest ε_r enhancement, a suppressed tanδ at audio frequencies, and no new relaxation below 1 MHz the ideal low-loss dielectric profile- strongest for Ni^{2+} and Mg^{2+}. Above the dilute limit, dopant clustering generates MWS heterogeneity with slow interfacial relaxation, raising the low-frequency tanδ. Cu^{2+} again deviates: Jahn–Teller dynamics add a dipolar loss channel. Alkali/ammonium insertion loosens the lattice and raises both ε_r and loss. In the stoichiometric branch, TGS-type adducts display order–disorder ferroelectricity with a large, anisotropic ε_r peaking near the 49 °C Curie temperature [15,17,18], precisely the property profile required for pyroelectric detection [36,37].

Frequency-resolved conductivity obeys the universal dielectric response, Eq. (10) [38,39,40,41] as the following:

$$\sigma_{ac}(\omega) = \sigma_{dc} + A\, \omega^s \quad (10)$$

where $\sigma_{ac}(\omega)$ the total frequency-dependent electrical conductivity measured at an angular frequency ω ($\omega = 2\pi f$), σ_{dc} the direct current (frequency-independent) conductivity and $A\omega^s$ The purely dispersive (frequency-dependent) component that dominates at higher frequencies (A is a temperature-dependent pre-exponential factor that determines the strength of polarizability and s is the frequency exponent).

The temperature dependence of the power-law exponent s discriminates the transport mechanism: correlated barrier hopping (CBH) gives Eq. (11) [42,43] as we see

$$s = 1 - 6\, k_B\, T / W_M \quad (11)$$

where here it finds $s < 1$ and decreases with temperature; quantum-mechanical tunnelling gives $s \approx 0.17–0.2$, temperature-independent; overlapping large-polaron tunnelling gives s increasing with temperature and W_M the maximum barrier height for correlated hopping. The dilute doped crystals are predicted to show s close to unity at room temperature with weak temperature dependence the signature of defect-pinned, short-range hops whereas undoped crystals containing mobile protonic carriers show steeper CBH-type dispersion. Thermally activated conduction follows Eq. (12); the extracted activation energy E_a separates protonic hopping (low E_a) from defect-mediated transport (higher E_a). Dielectric spectroscopy from 10 Hz to 1 MHz at 303–423 K is prescribed as the electrical acceptance test.

$$\sigma(T) = \sigma_0 \exp(-E_a / k_B\, T) \quad (12)$$

where k_B the Boltzmann constant, and σ_0 the pre-exponential factor [32,38,39,40,41,42,43].

7. Application-Specific Dopant Selection Rules

To anchor the proposed crystallochemical framework in empirical observations, Table 3 compiles representative structural, thermal, and dielectric benchmarks reported across isolated slow-evaporation studies of sulfate-bearing glycine crystals. Although variations in mother-liquor pH, supersaturation, and measurement frequencies preclude a single universal curve, the collective experimental trends corroborate the regime boundaries established in Sections 4–6: dilute Mg^{2+}, Zn^{2+}, and Ni^{2+} sulfates consistently stabilize the polar γ-polymorph while suppressing tanδ, whereas Cu^{2+} and monovalent alkali/ammonium sulfates introduce anisotropic strain or interfacial relaxation, and stoichiometric H_2SO_4 yields the distinct TGS ferroelectric branch.

Table 3. Comparative crystallochemical, thermal, and dielectric trends across slow-evaporation-grown sulfate-bearing glycine systems synthesized from the literature framework of Sections 3–6.

Optical / Functional Suitability	Dielectric & Conductivity Behavior	Thermal Stability & Decomposition Trend	Lattice & Defect Signature	Dominant Polymorph / Phase	Dopant / System
Reference polar NLO crystal (SHG active)	Steeper CBH-type protonic dispersion (s<1, temperature-dependent)	$T_d \approx 233 - 262$°C; baseline E_d	3D H-bonded 3_1 helical chains ($a = b = 7.035$ Å, $C = 5.481$ Å)	γ ($P3_1$)	Pure-γ glycine (Baseline)
Optimal for SHG (1064→ 532 nm) and frequency conversion	Modest ε_r enhancement; suppressed low-frequency tanδ; s→1	Elevated T_d (>233°C) and highest E_d via ionic cross-linking	Carboxylate-coordinated $\{M^{2+} \ldots SO_4^{2-}\}$ pairs; FWHM & δ minima	γ ($P3_1$)	$ZnSO_4$/$MgSO_4$ (0.5-1 mol%)

Optimal for low-loss dielectric microstructures & substrates	Strongest tanδ suppression; pinned carriers; no relaxation < 1 MHz	Enhanced E_d over pure γ-glycine	Lattice-compatible point defect (r = 0.69Å); minimal $\Delta d/d$	γ ($P3_1$)	(≤ 1 mol%) $NiSO_4$
Excluded from NLO/dielectrics (strain & visible d–d absorption)	Additional Jahn–Teller dipolar loss channel elevating tanδ	$E_d \approx E_d$ (pure γ); lower thermal reinforcement	Jahn–Teller (d^9) tetragonal elongation; anisotropic *hkl* broadening	γ ($P3_1$)	(Dilute) $CuSO_4$
Excluded from device-grade applications	Lattice loosening and MWS clustering; elevated ε_r and tanδ	Weakened H-bond network; lowest E_d among doped variants	Interlayer insertion (r=1.38−1.43 Å); measurable $\Delta d/d$ shift	or γ (strained) α	$(NH_4)_2$ SO_4/K_2SO_4
Optimal for pyroelectric IR detection (2–14μm) below 49℃	Order–disorder ferroelectricity; large anisotropic ε_r peaking at 49℃	Chemical stability ~ 230℃; ferroelectric Curie point T_C = 49℃	Distinct compound $(GlyH^+)(Gly^{\pm})_2$. HSO_4^-	Monoclinic adduct	Stoichiometric H_2SO_4 (TGS-type)

Figure 2 condenses the analysis into a dopant-concentration regime map, and Table 4 converts it into explicit selection rules by application. The logic couples each application's figure of merit to the property triad established above, and deliberately names excluded dopant classes as well as recommended ones.

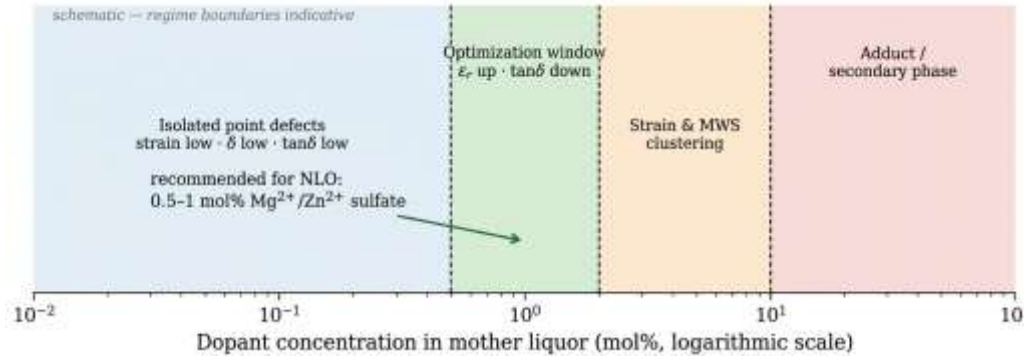


Figure 2: Schematic dopant-concentration regime map for sulfate-doped glycine grown by slow evaporation, summarizing the structural, thermal, and electrical analyses of Sections 4–6. The optimization window for device-grade doped crystals lies at 0.5–2 mol%; the stoichiometric branch corresponds to a distinct TGS-type compound rather than doped glycine.

For second-harmonic generation (1064 → 532 nm) and related frequency conversion, the requirements are: preserved non-centrosymmetry (γ phase), minimal microstrain for optical homogeneity and phase matching (Eq. (4)), large well-ordered crystallites (Eq. (3)), and a decomposition onset above all processing temperatures. Additionally, optical transparency across the fundamental and second-harmonic wavelengths must be verified via UV–Vis spectroscopy to ensure a low optical cut-off wavelength with negligible self-absorption at 532 nm, which reinforces the exclusion of Cu^{2+} due to its broad visible $d-d$ electronic absorption band. The recommended regime is γ-glycine doped with 0.5–1 mol% Mg^{2+} or Zn^{2+} sulfate, verified by the Kurtz–Perry powder SHG test [44] against the documented γ-glycine response [6,7,12] and by analogy with proven sulfate-bearing semiorganics such as ZTS [3]. Cu^{2+} (Jahn–Teller strain), alkali/ammonium salts (interlayer expansion disturbing the polar axis), and any regime beyond 2 mol% are excluded.

For pyroelectric infrared detection, the required combination is a large pyroelectric coefficient, a Curie point safely above the operating temperature, and low dielectric loss at the modulation frequency (10–100 Hz) [36]. Here, the stoichiometric glycine–sulfuric acid branch a TGS-type adduct, is the rational choice, because dilute defect doping of pure glycine cannot generate spontaneous polarization of comparable magnitude; the operating envelope should respect the 49 °C Curie temperature [15,17,18]. Internal-bias engineering through further chiral dopant substitution, documented for the TGS family [15,17], is compatible with this branch.

For low-loss dielectric microstructures, capacitive elements, and substrates for integrated optics, the priority inverts: minimal and temperature-stable tanδ with modest ε_r. The recommended regime is dilute (≤1 mol%) Ni^{2+} or Mg^{2+} sulfate; Cu^{2+} is excluded for its Jahn–Teller dipolar loss and alkali salts for MWS clustering. Finally, the framework prescribes what sulfate-doped glycine should not be used for: no variant is suitable for continuous service above ≈150 °C, because the organic lattice decomposes near 233 °C [6,7,8], and the metastable β phase should be avoided in all device roles.

Table 4. Application-specific dopant selection rules for sulfate-doped glycine crystals (this work).

Target application	Critical requirements	Recommended dopant regime	Choices to exclude	Rationale
Second-harmonic generation (1064 → 532 nm) and frequency conversion	Non-centrosymmetry (γ); low microstrain; large ordered crystallites; decomposition onset above processing temperatures	γ-glycine + 0.5–1 mol% Mg^{2+} or Zn^{2+} sulfate; verify by Kurtz–Perry SHG [29]	Cu^{2+}; K^+/NH_4^+ salts; any regime > 2 mol%; β phase	Strain and phase-purity logic of Sections 4–5 [3,7,12]
Pyroelectric infrared detection (2–14 μm)	Large pyroelectric coefficient; Curie point above ambient; low tanδ at 10–100 Hz	Stoichiometric glycine–H_2SO_4 adduct (TGS-type); operate below 49 °C [12,13]	Dilute divalent regimes (insufficient spontaneous polarization)	Order–disorder ferroelectricity of the adduct branch [15,16,36]
Low-loss dielectric microstructures	Minimal, temperature-stable tanδ; modest ε_r	≤1 mol% Ni^{2+} or Mg^{2+} sulfate	Cu^{2+} (Jahn–Teller dipolar loss); alkali salts (MWS clusters)	Pinned charge-neutral defect dipoles; suppressed carrier population (Section 6)
Continuous service above ≈150 °C	—	None	All sulfate-doped glycine variants	Organic lattice decomposes near 233 °C [7,8]

8. Conclusions

A unified theoretical comparison of sulfate-doped glycine crystals grown by slow evaporation has been constructed, connecting three incorporation channels to the structural, thermal, and electrical property triad through twelve quantitative relations. The central findings are threefold. First, divalent first-row sulfate dopants in the sub-2 mol% regime act as charge-neutral, lattice-compatible point defects that preserve the polar γ lattice while raising the decomposition onset and suppressing dielectric loss. Second, oversized alkali/ammonium sulfates and under- or over-doped regimes produce interlayer strain, MWS loss, and phase instability, and should not be used in device crystals. Third, the stoichiometric glycine–sulfuric acid branch is a separate ferroelectric material class, optimal for pyroelectric detection below its 49 °C Curie point.

The framework is deliberately prescriptive and falsifiable: a single experimental campaign powder XRD with Williamson–Hall analysis, sulfate-band FTIR, TGA/DSC at three heating rates, and 10 Hz–1 MHz dielectric spectroscopy tests all of its predictions. On this basis, Mg^{2+}- and Zn^{2+}-sulfate-doped γ-glycine are promoted as primary candidates for compact semiorganic nonlinear optical devices, Ni^{2+}/Mg^{2+}-doped crystals for low-loss dielectric roles, and TGS-type adducts for pyroelectric detection, each to the exclusion of the other dopant classes for these specific applications.

References

[1] Shirsat, R. K. (2025). Review of Semi Organic Nonlinear Optical (NLO) Crystals for Second-Harmonic Generation Applications. Int J Sci Res Sci Technol, 12(8), 759-764.

[2] D. S. Chemla, J. Zyss (Eds.), *Nonlinear Optical Properties of Organic Molecules and Crystals*, Vols. 1–2, Academic Press, Orlando, 1987.

[3] P. M. Ushasree, R. Jayavel, C. Subramanian, P. Ramasamy, Growth of zinc tris(thiourea) sulfate (ZTS) single crystals: a new semiorganic nonlinear optical material, *J. Cryst. Growth* 197 (1999) 216–220.

[4] V. Venkataramanan, S. Maheswaran, J. N. Sherwood, H. L. Bhat, Crystal growth and physical characterization of the semiorganic nonlinear optical material bis(thiourea)cadmium chloride, *J. Cryst. Growth* 179 (1997) 605–610.

[5] Zhang, L., Zhou, L., Hou, B., Yin, Q., & Xie, C. (2018). Synthesis, Growth, and Characterization of a New Thiourea and Bismuth Chloride Complex with Excellent Nonlinear Optical Properties. Transactions of Tianjin University, 24(6), 532-537.

[6] Pokorný, V., Štejfa, V., Havlín, J., Fulem, M., & Růžička, K. (2024). Heat Capacities of α-, β-, and γ-Polymorphs of Glycine. Molecules, 29(22), 5366.

[7] Y. Iitaka, The crystal structure of γ-glycine, *Acta Crystallogr.* 14 (1961) 1–10.

[8] Y. Iitaka, The crystal structure of α-glycine, *Acta Crystallogr.* 13 (1960) 35–45.

[9] Y. Iitaka, The crystal structure of β-glycine, *Acta Crystallogr.* 11 (1958) 225.

[10] R. E. Marsh, A refinement of the crystal structure of glycine, *Acta Crystallogr.* 11 (1958) 654.

[11] International Centre for Diffraction Data, Powder Diffraction File: α-glycine, Card No. 32-1702; γ-glycine, Card No. 06-0230, ICDD, Newtown Square, PA, USA.

[12] M. Narayan Bhat, S. M. Dharmaprakash, Growth of nonlinear optical γ-glycine crystals, *J. Cryst. Growth* 236 (2002) 376–380.

[13] CHANDAN, D. (2023). Ferroelectric Material Triglycine Sulphate (TGS): Properties, Synthesis, and Applications. INTERNATIONAL JOURNAL OF RESEARCH, (34), 50-63.

[14] Pandey, S. (2025). TGS Crystal Growth and Characterization (Doctoral dissertation, Netaji Subhas Institute of technology).

[15] B. T. Matthias, C. E. Miller, J. P. Remeika, Ferroelectricity of glycine sulfate, *Phys. Rev.* 104 (1956) 849–850.

[16] S. Hoshino, Y. Okaya, R. Pepinsky, Crystal structure of the ferroelectric phase of triglycine sulfate, *Phys. Rev.* 115 (1959) 323–329.

[17] M. E. Lines, A. M. Glass, *Principles and Applications of Ferroelectrics and Related Materials*, Clarendon Press, Oxford, 1977.

[18] F. Jona, G. Shirane, *Ferroelectric Crystals*, Pergamon Press, Oxford, 1962.

[19] Mailoud, O., & Driza, N. (2026). Curie Temperature and Single-Crystal Properties of Glycine Doped with Four Chloride Salts: A Landau–Devonshire Theoretical Study. AlQalam Journal of Medical and Applied Sciences, 3504-2511.

[20] Mei A. and Luo X. (2019). The structural, electronic and optical properties of γ-glycine under pressure: a first principles study. RSC Advances. 9, 3877–3883.

[21] R. D. Shannon, Revised effective ionic radii and systematic studies of interatomic distances in halides and chalcogenides, *Acta Crystallogr. A* 32 (1976) 751–767.

[22] P. Santhanaraghavan, P. Ramasamy, *Crystal Growth Processes and Methods*, KRU Publications, Coimbatore, 2000.

[23] P. Scherrer, Bestimmung der Grösse und der inneren Struktur von Kolloidteilchen mittels Röntgenstrahlen, *Nachr. Ges. Wiss. Göttingen, Math.-Phys. Kl.* 2 (1918) 98–100.

[24] Al-Sabaawy, M. H., Al-Jubouri, M. A. J., & Al-Saraj, M. S. (2025). Using Scherrer equation to calculate crystalline size from X-ray diffraction data of cement. Iraqi National Journal of Earth Science (INJES), 25(3), 31-43.

[25] Pal, A. (2025). A dimensionally consistent size–strain plot method for crystallite size and microstrain estimation. Journal of Alloys and Compounds, 185324.

[26] G. K. Williamson, W. H. Hall, X-ray line broadening from filed aluminium and wolfram, *Acta Metall.* 1 (1953) 22–31.

[27] Borbély, A. (2022). The modified Williamson-Hall plot and dislocation density evaluation from diffraction peaks. Scripta Materialia, 217, 114768.

[28] K. Nakamoto, *Infrared and Raman Spectra of Inorganic and Coordination Compounds*, Part A, 6th ed., John Wiley & Sons, Hoboken, 2009.

[29] Zhou, J., Santambrogio, G., Brümmer, M., Moore, D. T., Wöste, L., Meijer, G., ... & Asmis, K. R. (2006). Infrared spectroscopy of hydrated sulfate dianions. The Journal of chemical physics, 125(11).

[30] H. E. Kissinger, Reaction kinetics in differential thermal analysis, *Anal. Chem.* 29 (1957) 1702–1706.

[31] Vyazovkin, S. (2020). Kissinger method in kinetics of materials: things to beware and be aware of. Molecules, 25(12), 2813.

[32] P. Debye, *Polar Molecules*, The Chemical Catalog Company, New York, 1929.

[33] J. C. Maxwell, *A Treatise on Electricity and Magnetism*, Vol. 1, 2nd ed., Clarendon Press, Oxford, 1881.

[34] K. W. Wagner, Erklärung der dielektrischen Nachwirkungsvorgänge auf Grund Maxwellscher Vorstellungen, *Arch. Elektrotech.* 2 (1913) 371–387.

[35] R. W. Sillars, The properties of a dielectric containing semiconducting particles of various shapes, *J. Inst. Electr. Eng.* 80 (1937) 378–394.

[36] S. B. Lang, *Sourcebook of Pyroelectricity*, Gordon and Breach, London, 1974.

[37] Trybus, M., Chotorlishvili, L., & Jartych, E. (2024). Dielectric and magnetoelectric properties of TGS–magnetite composite. Molecules, 29(6), 1378.

[38] A. K. Jonscher, The "universal" dielectric response, *Nature* 267 (1977) 673–679.

[39] A. K. Jonscher, *Dielectric Relaxation in Solids*, Chelsea Dielectrics Press, London, 1983.

[40] Papathanassiou, A. N., & Sakellis, E. (2025). Compensation between the parameters of the Jonschers's Universal Dielectric Response Law in disordered materials. arXiv preprint arXiv:2505.18515.

[41] Karmakar, S., Patwari, M., Arun, S. V., Borkar, H., & Chakraborty, B. (2026). Revisiting Jonscher's universal power law: a modified formalism with Cole–Cole-type non-Debye dielectric relaxation for α-quartz-type GeO2. RSC advances, 16(41), 49127-49143.

[42] G. E. Pike, ac conductivity of chalcogenide glassy semiconductors, *Phys. Rev. B* 15 (1977) 2184.

[43] S. R. Elliott, A theory of ac conduction in chalcogenide glasses, *Philos. Mag.* 36 (1977) 1291–1304.

[44] S. K. Kurtz, T. T. Perry, A powder technique for the evaluation of nonlinear optical materials, *J. Appl. Phys.* 39 (1968) 3798–3813.

Disclaimer/Publisher's Note: The statements, opinions, and data contained in all publications are solely those of the individual author(s) and contributor(s) and not of **JIBAS** and/or the editor(s). **JIBAS** and/or the editor(s) disclaim responsibility for any injury to people or property resulting from any ideas, methods, instructions, or products referred to in the content.